Journal of Materials Chemistry A

Accepted Manuscript

ROYAL SOCIETY OF CHEMISTRY

www.rsc.org/materialsA

Journal Name

ARTICLE

Enhancement of oxygen reduction activities by Pt nanoclusters decorated on ordered mesoporous porphyrinic carbons

Received 00th January 20xx,
Accepted 00th January 20xx

DOI: 10.1039/x0xx00000x

www.rsc.org/

Sun-Mi Hwang,[a] YongMan Choi,[b] Min Gyu Kim,[c] Young-Jun Sohn,[a] Jae Yeong Cheon,[d] Sang Hoon Joo,[d,e] Sung-Dae Yim,[a] Kurian A. Kuttiyiel,[f] Kotaro Sasaki,[f] Radoslav R. Adzic,[f] and Gu-Gon Park*[a]

The high cost of Pt-based membrane electrode assembly (MEA) is a critical hurdle for the commercialization of polymer electrolyte fuel cells (PEFCs). Recently, non-precious metal-based catalysts (NPMCs) have demonstrated much enhanced activity but their oxygen reduction reaction (ORR) activity is still inferior to that of Pt-based catalyst resulting in much thicker electrode in the MEA. For the reduction of mass transport and ohmic overpotential we adopted a new concept of catalyst that combines ultra-low amount of Pt nanoclusters with metal-nitrogen (M-N_x) doped ordered mesoporous porphyrinic carbon (FeCo-OMPC(L)). The 5 wt% Pt/FeCo-OMPC(L) showed a 2-fold enhancement in activities compared to a higher loading of Pt. Our experimental results supported by first-principal calculations indicate that trace amount of Pt nanoclusters on FeCo-OMPC(L) significantly enhances the ORR activity due to its electronic effect as well as geometric effect from the reduced active sites. In terms of fuel cell commercialization, this class of catalyst is a promising candidate due to its limited use of Pt in the MEA.

Introduction

Polymer electrolyte fuel cells (PEFCs) have been recognized as an ideal electrical power system due to its eco-friendly and highly efficient energy conversion characteristics. However, the development of cost effective electrocatalyst by reducing or excluding the platinum in the fuel cell is one of the main challenges for the practical application of PEFCs.[1-7] After Jasinski's pioneering work about notable oxygen reduction reaction (ORR) activity on Co-phthalocyanine in alkaline medium,[8] the class of non-precious metal-based catalysts (NPMCs) has been receiving attention, especially the nitrogen coordinated transition metal (Fe and/or Co) doped carbon compounds (M-N_x-C).[9-40] The development of NPMCs with remarkable catalytic activity and stability towards the ORR rivaling those of Pt-based catalysts has been a challenging task as it requires fine tuning the composition of transition metal and nitrogen coordination number. The ORR activity of M-N_x-C catalysts strongly depends on the types of nitrogen and transition metal sources, heat treatment temperature, and graphiticity and morphology of carbon support, etc.[17-40] Even though the ORR activity and durability in alkaline media have been improved via the optimization of the synthetic process,[33, 34] the ORR activity in acid medium is still inferior to Pt-based electrocatalysts. Recently, Dodelet *et al.*[41] and Joo *et al.*[40] reported high ORR activity for NPMC, i.e. Fe- and/or Co-N-C catalyst and self-supported ordered mesoporous porphyrinic carbon (OMPC), which shows a commensurate ORR activity with Pt/C in acidic electrolyte using rotating disk electrode (RDE).

In terms of membrane electrode assembly (MEA) fabrication, however, NPMC-based MEA has around ten times thicker catalyst layer than that of conventional Pt/C MEA[41] due to high catalyst loading resulting in increased mass transport resistance as well as electrical resistance. The high ORR activity observed at a half-cell configuration could not be observed in NPMC-based MEA. Hence, decreasing the catalyst loading in the unit area may be important to obtain consistent performance in MEA, as shown in the RDE evaluation.

In this study, we evaluate a new concept that can enhance the ORR activity via using a low-amount of platinum nanocluster on NPMC (Pt/NPMC hybrid catalyst). The Pt/NPMC hybrid catalyst shows much enhanced ORR activity due to its electronic effect and also due to the geometric effect caused from dual active sites. The density-functional-theory (DFT) calculations suggest the mechanism of Pt cluster formation on the NPMC and also explain its positive effect on ORR that is constrained by its loading.

[a] *Fuel Cell Laboratory, Korea Institute of Energy Research (KIER), Daejeon 305-343, South Korea. *E-mail: gugon@kier.re.kr*
[b] *SABIC Technology Center, Riyadh 11551, Saudi Arabia.*
[c] *Pohang Accelerator Laboratory, Pohang 790-784, Republic of Korea.*
[d] *Department of Chemistry, Ulsan National Institute of Science and Technology (UNIST), Ulsan 689-798, South Korea.*
[e] *School of Energy and Chemical Engineering, Ulsan National Institute of Science and Technology (UNIST), Ulsan 689-798, South Korea.*
[f] *Chemistry Department, Brookhaven National Laboratory, Upton, New York 11973, USA.*
Electronic Supplementary Information (ESI) available: See
DOI: 10.1039/x0xx00000x

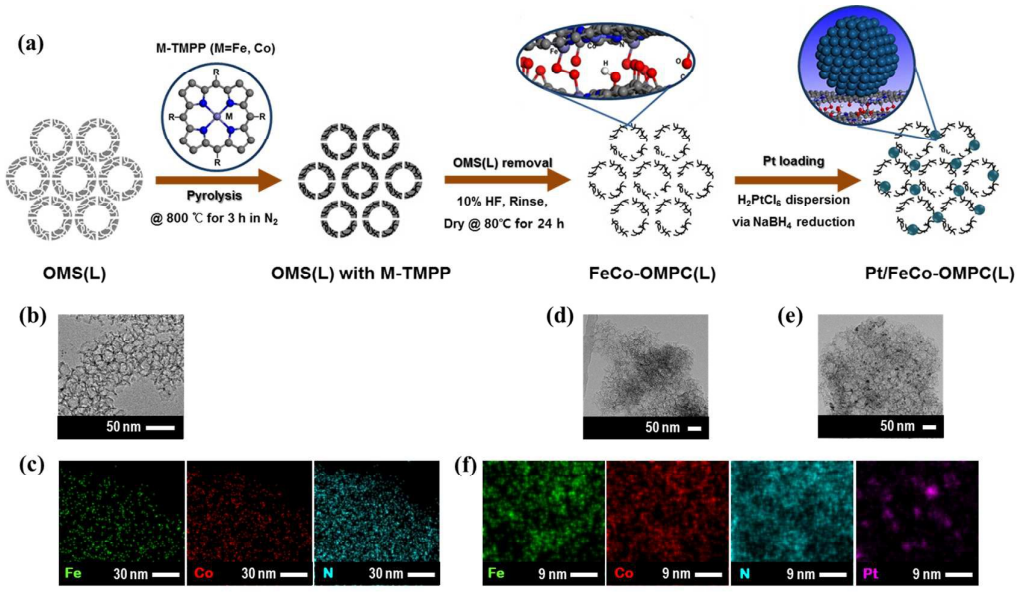

Fig. 1 (a) Synthesis process of Pt/FeCo-OMPC(L), (b) TEM image of ordered mesoporous silica template with 20 nm large mesopores (OMS(L)), (c) EDS mapping images of FeCo-OMPC(L), TEM images of (d) FeCo-OMPC(L) and (e) 5 wt% Pt/FeCo-OMPC(L), and (f) EDS mapping images of 5 wt% Pt/FeCo-OMPC(L).

Results and discussion

Figure 1(a) shows schematic of the synthesis procedure of Pt/FeCo-OMPC(L) via nanocasting method using large pore OMS(L) hard template (Fig. 1(b)) and $NaBH_4$ reduction. EDS mapping images for FeCo-OMPC(L) (Fig. 1(c)) show uniformly distributed Fe, Co, and N elements in the mesoporous carbon structures with a 7-8 nm pore size (Fig. 1(d)). The FeCo metallic nanoparticles were removed by the HF washing procedure. The final FeCo-OMPC(L) consisted of 1.63 wt% Fe, 1.47 wt% Co, and 6.8 wt% N, as summarized in Table 1. Pt nanoclusters were well distributed on FeCo-OMPC(L) as shown in Fig. 1(e). EDS mapping images for Pt/FeCo-OMPC(L) catalyst as shown in Fig. 1(f) clearly demonstrates the presence of Fe, Co and N elements along with some Pt clusters. The average Pt particle sizes calculated with Pt(111), (200), (220) diffraction peaks from XRD were 2.1 nm for Pt/FeCo-OMPC(L), 3.5 nm for Pt/OMPC(L), and 6.8 nm for Pt/C, respectively (Table S1). Pt lattice fringe was observed with (111) spacing of 2.27 Å ($Pt_{111,bulk}$=2.26 Å) that is in good agreement with the 2.26 Å calculated from Pt(111) diffraction peaks. The metal contents in the Pt/FeCo-OMPC(L) catalysts were summarized in Table 1. The Fe, Co, and N elemental composition shows a slight change in weight content before and after Pt loading by $NaBH_4$ reduction.

Figure 2(a) shows the ORR polarization curves for the as-prepared catalysts measured in 0.1 M $HClO_4$ using the RDE technique. The half-wave potential on 5% Pt/FeCo-OMPC(L) was 858 mV vs. RHE which was 13 mV and 103 mV higher than that of 5% Pt/OMPC(L) and 5% Pt/C catalysts, respectively. The Pt/FeCo-OMPC(L) showed 1.4 and 8.3-fold enhanced kinetic current density (j_k) compared to Pt/OMPC(L) and Pt/C at 0.9 V vs. RHE, respectively (Table S1). The specific activity (j_s) and

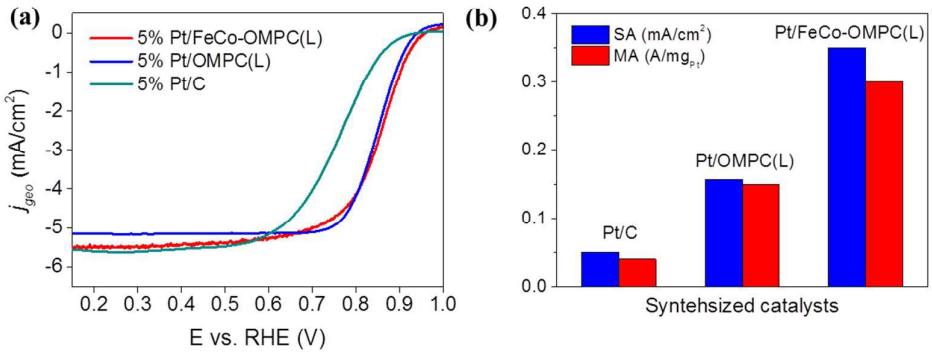

Fig. 2 (a) Polarization curves for the ORR on prepared 5% Pt/FeCo-OMPC(L) (4.49 $\mu g_{Pt}/cm^2$), 5% Pt/OMPC(L) (6.22 $\mu g_{Pt}/cm^2$), and 5% Pt/C (3.88 $\mu g_{Pt}/cm^2$) catalysts in O_2-saturated 0.1 M $HClO_4$ with a sweep rate of 10 mV/s at 1600 rpm (total catalyst loading is 84 $\mu g_{catalyst}/cm^2$) and (b) comparison of mass and specific activities at 0.9 V vs. RHE.

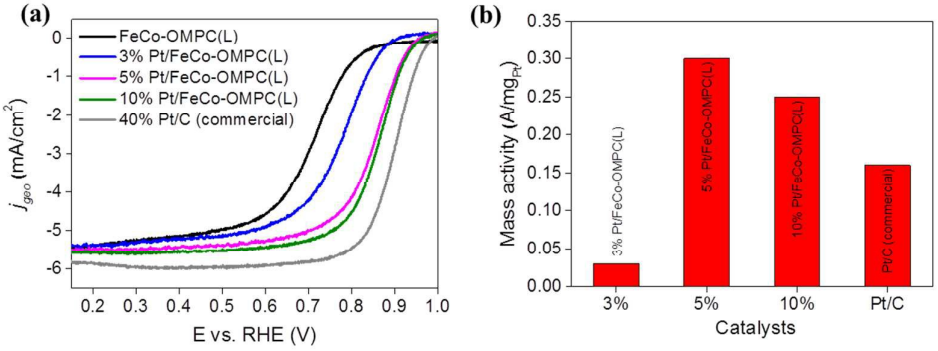

Fig. 3 Polarization curves for the ORR on FeCo-OMPC(L), 3% Pt/FeCo-OMPC(L) (2.30 $\mu g_{Pt}/cm^2$), 5% Pt/FeCo-OMPC(L) (4.49 $\mu g_{Pt}/cm^2$), 10% Pt/FeCo-OMPC(L) (6.63 $\mu g_{Pt}/cm^2$), and 40% Pt/C (34 $\mu g_{Pt}/cm^2$) electrocatalysts in O_2-saturated 0.1 M $HClO_4$ with a sweep rate of 10 mV/s at 1600 rpm (total catalyst loading is 84 $\mu g_{catalyst}/cm^2$) and (b) comparison of mass activities at 0.9 V vs. RHE.

mass activity (j_m) for Pt/FeCo-OMPC(L) were also improved by a factor of 2 and 7 relative to those of Pt/OMPC(L) and Pt/C at 0.9 V, respectively (Fig. 2(b)). This change in ORR activity is clearly due to interaction between Pt nanoclusters and the support. The ORR activity of the support catalysts followed the same order; FeCo-OMPC(L) > OMPC(L) > Vulcan XC-72 (VC) (Fig. S1).

A substantial increase in the ORR activity was observed with the introduction of Pt nanoclusters on the FeCo-OMPC(L) (Fig. 3(a)). The positive shift of half-wave potential ($E_{1/2}$) was an evidence for the enhancement of ORR activity with the different Pt loading on the FeCo-OMPC(L) support. The ORR kinetics current density (j_k), corrected for diffusion-limited current, increased by a factor of 9 for 5 wt% Pt/FeCo-OMPC(L) compared to that of FeCo-OMPC(L) at 0.9 V vs. RHE. When the Pt-based mass activity (j_m) was compared with commercial 40 wt% Pt/C catalyst, 5 wt% Pt/FeCo-OMPC(L) showed ca. 2-fold enhanced mass activity (j_m) at 0.9 V as shown in Fig. 3(b) and Table S1. Electrochemical surface area (ECSA) of Pt measured by CO stripping increased with Pt metal loading, however, the overall ORR activity was not linearly improved in accordance with the amount of the Pt nanoclusters on the FeCo-OMPC(L).

The above results suggest that the enhancement of the ORR activity on Pt/FeCo-OMPC(L) can be attributed to not only dual active sites but also the electronic effect between Pt nanoparticles and FeCo-OMPC(L). Prior to figuring out the electronic effect, we carefully considered the dual active site effect originating due to the loading of Pt on FeCo-OMPC(L) support. The high surface area of FeCo-OMPC(L) is one of the main factors for the high activity towards the ORR. However, we did observe that a surface area of the Pt/FeCo-OMPC(L) catalysts decreased from 970 to 458 m^2/g with an increase in Pt loading, as plotted in Fig. 4. Decrease in the surface area of Pt/FeCo-OMPC(L) can be explained by blocking of the mesopores and micropores in the FeCo-OMPC(L) by 2-3 nm Pt nanoclusters as well as by the different density of materials. Total pore volume of the catalysts was also decreased from 1.78 to 1.06 cm^3/g with an increase in the Pt loading amount. In other words, the activity loss of the 10 wt% Pt/FeCo-OMPC(L) may be caused by the decrease of the absolute number of active site. Therefore, the activity enhancement due to the increase in Pt loading was limited by the loss of FeCo-OMPC(L) active area caused by the increase in the number of Pt nanoclusters.

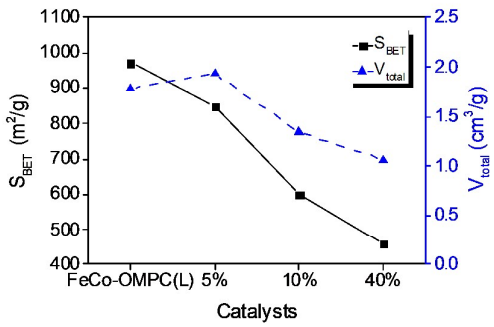

Fig. 4 (a) Trends of surface area and total pore volume of Pt/FeCo-OMPC(L) obtained from N_2 adsorption/desorption isotherms.

In order to understand the electronic effect between the Pt nanoclusters and transition metals (Fe and/or Co) or N in FeCo-OMPC(L) we carried out XPS, *in situ* EXAFS analyses and DFT calculations. Figure 5 shows the XPS result for the FeCo-OMCP(L) and 5%, 10% Pt/FeCo-OMPC(L) catalysts. The N 1s XPS spectrum for all catalysts indicate three dominant nitrogen species at 398.6, 400.1, 401.5 and 404 eV associated with pyridinic N (N1), pyrrolic N (N2), graphitic N (N3) and pyridine-N-oxide, respectively.[25] Binding energy (BE) shift to lower energy was observed for the pyrrolic N (-0.17 eV) and graphitic N (-0.43 eV) peaks for 5 wt% Pt/FeCo-OMCP(L) relative to N2 (pyrrolic N) and N3 (graphitic N) peaks for FeCo-OMPC(L) which is associated with modification of electronic structure of N site binding with Fe or Co. In contrast, minor BE shift to higher energy was examined for pyridinic N (+0.04 eV) peaks for the catalyst. As the Pt loading increased, lower shift of BE for Pt $4f_{7/2}$ was observed indicating an increase in Pt-Pt interaction. The XPS results showed that the electronic structures of Pt nanoclusters on FeCo-OMPC(L) were modified by N elements connected with transition metals in the FeCo-OMPC(L).

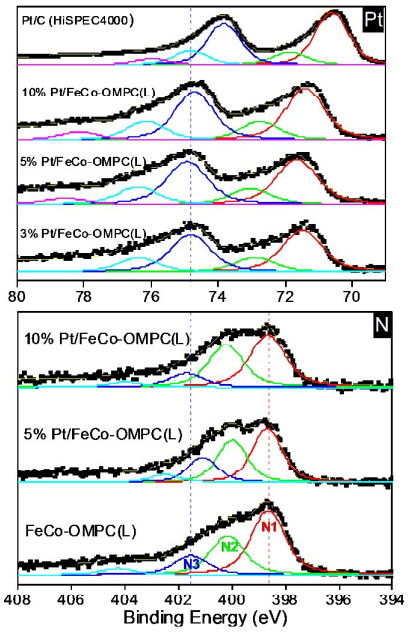

Fig. 5 XPS spectrums of N1s, Pt4f$_{7/2}$ for FeCo-OMPC(L), 3% Pt/FeCo-OMPC(L), 5% Pt/FeCo-OMPC(L), 10% Pt/FeCo-OMPC(L), and commercial Pt/C.

We investigated the effect of Pt nanoclusters on the electronic structure of the FeCo-OMPC(L) with *in situ* XAFS analysis. *In situ* XAFS analysis was performed at constant potential mode (0.3 V vs. RHE) to eliminate the oxygen molecule coordinated with the central Fe and/or Co in the axial direction and the surface of Pt in the Pt/FeCo-OMPC(L). The XANES spectra revealed that the square planar D_{4h} structure of Co-TMPP and Fe-TMPPCl compounds was broken down or distorted in the FeCo-OMPC(L) catalyst during the pyrolysis process at high temperatures (Fig. S2). The FT EXAFS for Fe k-edge, Co k-edge of FeCo-OMPC(L) indicated no existence of Fe or Co metallic phase in the FeCo-OMPC(L) structure which is in good agreement with the TEM-EDS mapping images (Fig. 6(b) and 6(c)). There is no evident FT peaks related with Pt-TM coordination (TM=Fe, Co), whereas Pt-N coordination was observed at around 1.93 - 2.01 Å from FT EXAFS for Pt L_3-edge, as shown in Fig. 6(a). The peak intensity for Pt-N coordination decreased with an increase in Pt amount in the Pt/FeCo-OMPC(L). This means that the Pt nanoclusters are mainly positioned at near N-site and the interaction between Pt nanoclusters and N becomes weaker

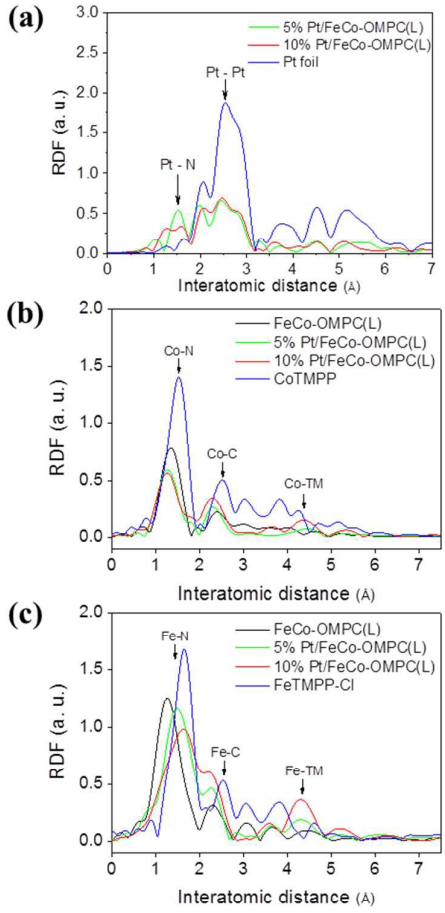

Fig. 6 Fourier-transform (FT) EXAFS of Fe k-edge, Co k-edge, and Pt L_{III}-edge from in-situ XAFS analysis under potentiostatic condition at 0.3 V vs. RHE for FeCo-OMPC(L), 5% Pt/FeCo-OMPC(L), 10% Pt/FeCo-OMPC(L) catalysts, and Pt foil reference, and CoTMPP, FeTMPPCl precursors.

with an increase in the Pt loading in the Pt/FeCo-OMPC(L) catalysts. A slight elongation of Fe-N distance was observed, whereas the Co-N distance had no big change with Pt contents.

To understand the mechanism of Pt nanocluster formation on FeCo-OMPC(L) and ORR activity enhancement by Pt nanoclusters, we carried out DFT calculations using the FeCo-OMPC(L) bulk structure consisting of 152 atoms (120 C, 12 N, 14 O, 2 Fe, 2 Co, and 2 H). As discussed earlier, the EXAFS analysis clearly revealed no interaction between Pt and the metal centers on Pt/FeCo-OMPC(L) catalyst. To propose a

Table 1 Composition of synthesized FeCo-OMPC(L), 5% Pt/FeCo-OMPC(L), and 10% Pt/FeCo-OMPC(L) catalysts analyzed by ICP-AES and EA

	FeCo-OMPC(L) (wt.% / at.%)	5% Pt/FeCo-OMPC(L) (wt.% / at.%)	10% Pt/FeCo-OMPC(L) (wt.% / at.%)
Pt	-	5.31 / 0.36	7.85 / 0.54
Fe	1.63 / 0.36	1.63 / 0.38	1.49 / 0.36
Co	1.47 / 0.31	1.33 / 0.30	1.10 / 0.25
N	6.80 / 6.04	5.90 / 5.51	5.10 / 4.87
C	90.10 / 93.29	85.83 / 93.46	84.46 / 93.99

plausible model and mechanism for the Pt nanocluster formation on FeCo-OMPC(L), we prepared the FeCo-OMPC(L) bulk structure, similar to the previous study (Fig. S3).[40] The model using the PBE exchange-correlation functional is in good agreement with the EXAFS and HRTEM results, such as the interlayer distance (Expt.: 4.77 Å and DFT: ~4.5 Å).[40] To match with the averaged coordination number of M-N (N = 3.3) for FeCo-OMPC(L) in Table 2, we kept N = 3 by removing one coordinated N with each metal center. Also, the M-N distances of the bulk model are in agreement with experiment (Co-N: 1.84 Å versus 1.76 Å and Fe-N: 1.83 Å versus 1.74 Å) (Table 2 and S2). Using the bulk structure, the C, N, Fe, and Co-terminated (0001) surface was generated for the surface calculations (Fig. S4) Then, we calculated the vacancy formation energies for the metal centers. As summarized in Table S2, the Co site can be more easily removed than the Fe site (6.09 eV/atom versus 6.74 eV/atom, respectively). Especially, the strong incorporation strength of Pt into the vacancy indicates that the first step of the Pt nanocluster formation on FeCo-OMPC(L) may be the incorporation process on the surface vacancy after leaching out of unstable surface metal centers. The essential energy can be provided by the exothermic reduction reaction using $NaBH_4$ as discussed in the experimental section. We observed that the Fe-N distance is lengthened by 2.2 % after the addition of Pt (DFT: 1.84 Å versus 1.87 Å and Expt.: 1.74 Å versus 1.92 - 1.99 Å (Table 2 and S3)). Also, the calculated distances of Pt-N and Pt-Pt for Pt_{19}/FeCo-OMPC(L) support experiment (DFT: 1.97 Å versus 2.64 Å, respectively, and Expt.: 1.93 – 2.01 Å versus 2.85 – 2.86 Å) (Table 2 and S3). According to the reasonable agreement with the modeling and experimental results, we propose a mechanism of the growth of Pt nanoclusters on FeCo-OMPC(L). As shown in Fig. 7 and S5, the first step is the removal of unstable surface metal centers, preferentially Co, and the incorporation of Pt into the metal-center vacancy. Then, the subsequent Pt nanocluster growth may occur via the linkage of the replaced Pt center (Fig. S5). It is desirable to execute more size-dependent studies, but due to high computational time, we optimized only two cases of Pt_6 and Pt_{19} (Fig. S6). It was found that the adsorption energy of Pt nanoclusters becomes weakened as the nanoclusters grow (Pt_6: –5.21 eV and Pt_{19}: –4.31 eV). Using the perfect FeCo-OMPC(L) model, we found that the longitudinal M-M distances range from ~0.8 to 1.5 nm. Thus, if we assume that the Pt nanoclusters of ~2 nm in diameter is sphere-like, the possibility to link Pt and the metal center is low within the calculated M-M distance range, supporting the EXAFS's analysis. In addition to the mechanistic study, we calculated BO by placing one oxygen atom only at the Fe metal center on the surface because of the surface ($Pt/FeCo\text{-}OMPC(L)_{def}$) doesn't have the

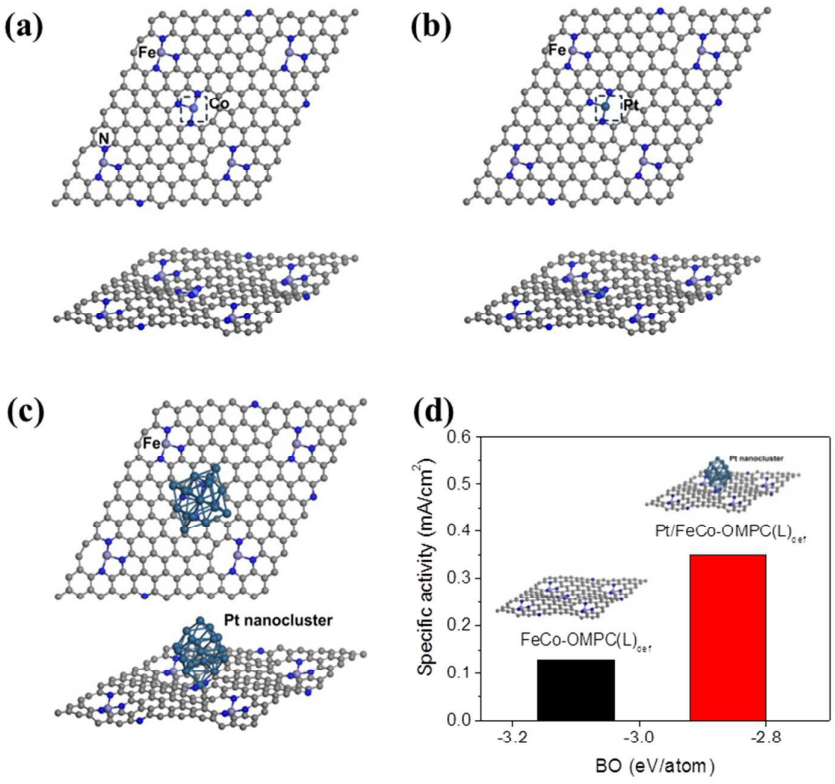

Fig. 7 Schematic illustration of FeCo-OMPC(L) surfaces (a) before and (b) after the replacement of Co to Pt and (c) after the Pt nanocluster formation. For clarity, only the topmost layer is shown, and (d) DFT results of specific activities versus calculated binding energy of atomic oxygen (BO) on the Fe center without and with the Pt nanocatalyst.

Table 2 The structural parameters obtained from FT EXAFS curve-fitting process for the Fe, Co K-edge k^2-weighted in-situ EXAFS spectra of the FeCo-OMPC(L), 5% Pt/FeCo-OMPC(L), and 10% Pt/FeCo-OMPC(L) catalysts

Edge	Path	Catalysts	R (Å)[a]	N[b]
Co K-edge	Co-N	FeCo-OMPC(L)	1.76	2.4
		5% Pt/FeCo-OMPC(L)	1.72	1.6
		10% Pt/FeCo-OMPC(L)	1.72	1.7
Fe K-edge	Fe-N	FeCo-OMPC(L)	1.74	4.2
		5% Pt/FeCo-OMPC(L)	1.92	3.7
		10% Pt/FeCo-OMPC(L)	1.99	3.2
Pt L_3-edge	Pt-N	5% Pt/FeCo-OMPC(L)	1.93	-
		10% Pt/FeCo-OMPC(L)	2.01	-
	Pt-Pt	5% Pt/FeCo-OMPC(L)	2.85	7.6
		10% Pt/FeCo-OMPC(L)	2.86	7.4

(a: bond distance, b: coordination number)

Co metal center. The Pt/FeCo-OMPC(L)$_{def}$ catalyst (–2.86 eV) showed a slight decrease in BO from that of FeCo-OMPC(L)$_{def}$ (–3.10 eV), indicating an enhanced ORR activity by the Pt nanocluster on FeCo-OMPC(L) (Fig. 7(d)).

From the results, we verified that the enhancement of the ORR mass activity on Pt/FeCo-OMPC(L) was attributed to both the electronic effect and the geometric effect caused by dual active sites of Pt nanoclusters and FeCo-OMPC(L). Therefore, the best electrochemical activity towards ORR was exhibited on 5 wt% Pt/FeCo-OMPC(L) considering the complementary effect between the absolute number of the active sites and electronic effect.

Conclusions

We reported a new approach for the enhanced ORR activity as well as the reduction of the precious metal utilization for fuel cell commercialization. We have synthesized a new class of electrocatalysts consisting of a trace amount of Pt nanoclusters on M-N doped ordered mesoporous porphyrinic carbon to enhance the intrinsic catalytic activity. The FeCo-OMPC(L) itself exhibits ORR activity due to its nitrogen coordinated metal centers, however, by adding low amount of Pt nanoclusters on FeCo-OMPC(L), much improved ORR activity could be obtained. Both the electronic and geometric effects were observed as the reason of activity enhancement. The 5 wt% Pt/FeCo-OMPC(L) electrocatalyst indicated a factor of two improvement in the ORR mass activity compared to Pt/C. The FeCo-OMPC(L) Pt loaded catalysts greater than 5 wt% showed decreased mass activities because of the reduced electronic effect and the shrunken absolute number of active sites caused by increased Pt particle size and density.

Experimental

Material synthesis

Nitrogen coordinated transition metal based ordered mesoporous carbon was synthesized by a nanocasting method.[40, 42-44] Ordered mesoporous silica (OMS(L)) templates with ca. 20 nm large mesopores were well mixed with 5,10,15,20-tetrakis(4-methoxyphenyl)-21H,23H-porphine iron(III) chloride (Fe-TMPPCl, Porphyrin Systems) and 5,10,15,20-tetrakis(4-methoxyphenyl)-21H,23H-porphine cobalt(II) (Co-TMPP, Porphyrin Systems) as a metallo-porphyrinic precursors, then the mixture was pyrolyzed at 800 °C for 3 h in N_2 atmosphere. The silica templates and metal particles in the composite were removed by washing in 10% HF solution, then the resulting FeCo-OMPC(L) was washed with deionized water for several times, followed by drying at 80 °C overnight. The OMPC(L) without transition metals was also prepared with 5,10,15,20-tetrakis(4-methoxyphenyl)-21H,23H porphyrin (TMPPH, Porphyrin Systems) and OMS(L) template under the same pyrolysis condition as described before.[40] Pt/FeCo-OMPC(L) electrocatalysts with various Pt loading were prepared by sodium borohydride ($NaBH_4$) reduction method.[45-47] FeCo-OMPC(L) was well dispersed in DI-based H_2PtCl_6 (37.5% Pt basis, ACS reagent, Aldrich) solution, then excess of 0.5 M $NaBH_4$ (98%, JUNSEI) solution was added drop by drop into the mixture with vigorous stirring for the complete reduction of the $PtCl_6^{2-}$ ion to Pt metal. The mixture was stirred for 24 h at ambient temperature, and washed with excess deionized water and dried at 80 °C for 24 h. For the direct comparison of ORR activities, catalysts that have the same Pt loading (5 wt%) were prepared by using FeCo-OMPC(L), OMPC(L) and Vulcan XC-72 as supports using the same procedures.

Characterization

The morphology and distribution of Pt nanoclusters in the Pt/FeCo-OMPC(L), Pt/OMPC(L), and Pt/C catalysts were examined by field emission transmission electron microscope (FE-TEM, Tecnai TF30 ST, FEI). High-angle annular dark field (HAADF) images and EDS-mapping of FeCo-OMPC(L) and Pt/FeCo-OMPC(L) was observed by Titan Double Cs corrected TEM (Titan cubed G2 60-300, FEI). X-ray diffraction (XRD, D/MAX-2500, RIGAKU) patterns of the prepared catalysts were obtained to calculate the Pt particle size using Scherrer's equation. The surface area and the pore size distribution of the catalysts were measured by N_2 adsorption-desorption isotherms (ASAP-2020, Micrometrics). The metal contents of Pt, Fe, and Co were measured by inductively coupled plasma atomic emission spectroscopy (ICP-AES), and the composition of C and N elements was examined with elemental analyzer (EA). X-ray photoelectron spectroscopy (XPS) was performed on AXIS NOVA with monochromated Cu K_α X-ray source.

In situ electrochemical cell for X-ray absorption spectroscopy (XAS) analysis was specially designed to operate at potentiostatic mode. Teflon based *in situ* XAS cell was mounted on a goniometer stage passivated implanted planar silicon (PIPS, Canberra Co.) and the fluorescence detector was positioned on top of the electrochemical cell (Fig. S7). XAS signals of Fe k-edge, Co k-edge, and Pt L_3-edge for the catalysts were recorded in fluorescence mode on the BL10C beam line at the Pohang Light Sources (PLS) with a ring current of 200 mA at 3.0 GeV. The monochromatic X-ray beam could be obtained using a liquid nitrogen-cooled Si (111) double crystal monochromator. Working electrode for the *in situ* XAS analysis was prepared by spray coating the Nafion containing catalyst ink onto the Nafion 117 membrane. Precise energy calibration was simultaneously carried out for each measurement with each reference metal foil placed in front of the third ion chamber using partially-bypassed X-ray beam. The data processing of the experimental spectra to normalized XANES and Fourier-transform (FT) EXAFS were performed through the standard XAFS procedure.[48-51]

Electrochemical analysis

The ORR kinetics on Pt/FeCo-OMPC(L) catalysts were examined using rotating disk electrode (RDE) method in a typical three-electrodes cell with a Pt counter electrode and hydrogen reference electrode (Gaskatel GmbH, Germany). The catalyst ink was prepared by sonication of 30 mg of Pt/FeCo-OMPC(L) in 1.2 ml of ethanol (10 ml) and DI (1 ml) mixture with 0.02 ml of 5wt% Nafion solution. A catalyst ink was pipetted onto a glassy carbon (GC, 0.196 cm^2) disk electrode mounted on the inverted rotator under rotating at 300 rpm to make uniform thin film, then dried under rotation for 20 min at room temperature.[52] The total amount of catalyst loading was 84 $\mu g_{catalyst}/cm^2$, but the Pt mass loading was dependent on the Pt contents in the Pt/FeCo-OMPC(L). The catalyst film coated on the GC electrode was cleaned and activated in nitrogen saturated 0.1 M $HClO_4$ (70%, ACS reagent, Aldrich) electrolyte by cyclic voltammetry between 0 V and 1.2 V vs. RHE with a scan rate of 100 mV/s for 50 cycles until obtaining quasi steady-state I-V characteristic. The ORR kinetics was examined by linear sweep voltammetry (LSV) using anodic sweep from 0.05 V to 1.15 V vs. RHE with a sweep rate of 10 mV/s in oxygen saturated 0.1 M $HClO_4$ as a function of RDE rotation rates from 400 rpm to 2,500 rpm.

DFT calculation

Periodic plane-wave DFT calculations were performed using the Vienna ab initio simulation package (VASP)[53,54] with projector augmented wave (PAW) potentials[55] and the Perdew-Burke-Ernzerhof (PBE) exchange-correlation functional.[56] The spin-polarization method was used in the calculations to correctly account for magnetic properties. Monkhorst-Pack[57] mesh **k**-points of (3 × 3 × 3) and (3 × 3 × 1) for bulk and surface calculations, respectively, were used. The plane-wave cutoff energy was optimized at 415 eV. To describe the interaction between Pt cluster and surface, adsorption energy is defined as E_{ads} = E[Pt_n/surface]– E[Pt_n] – E[surface], where E[Pt_n/surface], E[Pt_n], and E[surface] are the calculated electronic energies of adsorbed Pt_n on a surface, pure Pt_n cluster, and a clean surface, respectively. Also, we calculated the binding energy of atomic oxygen (BO) as a descriptor for scaling the ORR activity.[58-60] BO is defined as BO = E[O/surface] − E[surface] − E[O], where E[O/surface] and E[O], respectively, are the calculated electronic energies of adsorbed oxygen atom on a surface and a triplet oxygen atom. Since the topmost layer's Co metal center of the surface model of Pt/FeCo-OMPC(L) (Fig. S4) was replaced by Pt to support the experimental observation using the EXAFS analysis, we compared BO only on the Fe metal center. The vacancy formation energy of the metal center[61] is defined as $E_{M\text{-}vac}$ = E[d-surface] + E[M] – E[p-surface], where d-surface and p-surface are the surfaces with and without an M vacancy (M = Co or Fe). In this study, we used gas-phase atomic metals' energies by considering the number of their unpaired electrons. Incorporation energy of Pt into the vacancy of the metal centers is calculated by $E_{Pt\text{-}incorp}$ = E[Pt-surface] – E[Pt] – E[d-surface], where Pt-surface is the surface after incorporation of Pt into the M vacancy. Similar to the previous study,[40] the surface calculations on the perfect FeCo-OMPC(L) surface were first carried out on a C, N, and M-terminated (0001) plane (120 C, 12 N, 14 O, 2 Fe, 2 Co, and 2 H atoms) based on its bulk structure (Fig. S3) with a vacuum space of 10 Å. Only the bottom bilayer of the 2-layer FeCo-OMPC(L) surface was fixed, and the top bi-layer and the adsorbates were fully relaxed. Then, the M metal center on the topmost layer was removed and replaced by Pt to examine the vacancy formation and incorporation energies.

Acknowledgements

This research was supported by the New & Renewable Energy Core Technology Program of the Korea Institute of Energy Technology Evaluation and Planning (KETEP) granted financial resource from the Ministry of Trade, Industry & Energy,

Republic of Korea (No. 20133030011320) and Research and Development Program of the Korea Institute of Energy Research (KIER) (B5-2422-02).This work was also performed in collaboration with Brookhaven National laboratory under contract no. DE-SC0012704. DFT calculations were performed at KAUST Supercomputing Laboratory and the National Energy Research Scientific Computing Center (Contract No. DE-AC02-05CH11231).

Notes and references

1 M. K. Debe, *Nature*, 2012, **486**, 43-51.
2 H. A. Gasteiger, S. S. Kocha, B. Sompalli and F. T. Wagner, *Appl. Catal. B: Environ.*, 2005, **56**, 9-35.
3 H. A. Gasteiger and N. M. Markovic, *Science*, 2009, **324**, 48-49.
4 A. Morozan, B. Jousselme and S. Palacin, *Energy Environ. Sci.*, 2011, **4**, 1238-1254.
5 A. Brouzgou, S. Q. Song and P. Tsiakaras, *Appl. Catal. B: Environ.*, 2012, **127**, 371-388.
6 Y. Nie, L. Li and Z. Wei, *Chem. Soc. Rev.*, 2015, **44**, 2168-2201.
7 V. R. Stamenkovic, B. S. Mun, M. Arenz, K. J. J. Mayrhofer, C. A. Lucas, G. Wang, P. N. Ross and N. M. Markovic, *Nat Mater*, 2007, **6**, 241-247.
8 R. Jasinski, *Nature*, 1964, **201**, 1212-1213.
9 R. Bashyam and P. Zelenay, *Nature*, 2006, **443**, 63-66.
10 Z. Chen, D. Higgins, A. Yu, L. Zhang and J. Zhang, *Energy Environ. Sci.*, 2011, **4**, 3167-3192.
11 F. Jaouen, E. Proietti, M. Lefevre, R. Chenitz, J.-P. Dodelet, G. Wu, H. T. Chung, C. M. Johnston and P. Zelenay, *Energy Environ. Sci.*, 2011, **4**, 114-130.
12 G. Liu, X. Li, J.-W. Lee and B. N. Popov, *Catal. Sci. Technol.*, 2011, **1**, 207-217.
13 K. N. Wood, R. O'Hayre and S. Pylypenko, *Energy Environ. Sci.*, 2014, **7**, 1212-1249.
14 H. Wang, T. Maiyalagan and X. Wang, *ACS Catal.*, 2012, **2**, 781-794.
15 C. W. B. Bezerra, L. Zhang, K. Lee, H. Liu, A. L. B. Marques, E. P. Marques, H. Wang and J. Zhang, *Electrochim. Acta*, 2008, **53**, 4937-4951.
16 R. Othman, A. L. Dicks and Z. Zhu, *Int. J. Hydrog. Energy*, 2012, **37**, 357-372.
17 M. Lefèvre, E. Proietti, F. Jaouen and J.-P. Dodelet, *Science*, 2009, **324**, 71-74.
18 G. Wu, M. Nelson, S. Ma, H. Meng, G. Cui and P. K. Shen, *Carbon*, 2011, **49**, 3972-3982.
19 G. Wu, K. L. More, C. M. Johnston and P. Zelenay, *Science*, 2011, **332**, 443-447.
20 G. Wu, C. M. Johnston, N. H. Mack, K. Artyushkova, M. Ferrandon, M. Nelson, J. S. Lezama-Pacheco, S. D. Conradson, K. L. More, D. J. Myers and P. Zelenay, *J. Mater. Chem.*, 2011, **21**, 11392-11405.
21 F. Charreteur, F. Jaouen, S. Ruggeri and J.-P. Dodelet, *Electrochim. Acta*, 2008, **53**, 2925-2938.
22 C. Médard, M. Lefèvre, J. P. Dodelet, F. Jaouen and G. Lindbergh, *Electrochim. Acta*, 2006, **51**, 3202-3213.
23 F. Jaouen, M. Lefèvre, J.-P. Dodelet and M. Cai, *J. Phys. Chem. B*, 2006, **110**, 5553-5558.
24 A. Bonakdarpour, M. Lefevre, R. Z. Yang, F. Jaouen, T. Dahn, J. P. Dodelet and J. R. Dahn, *Electrochem. Solid State Lett.*, 2008, **11**, B105-B108.
25 F. Jaouen, J. Herranz, M. Lefèvre, J.-P. Dodelet, U. I. Kramm, I. Herrmann, P. Bogdanoff, J. Maruyama, T. Nagaoka, A. Garsuch, J. R. Dahn, T. Olson, S. Pylypenko, P. Atanassov and E. A. Ustinov, *ACS Appl. Mater. Interfaces*, 2009, **1**, 1623-1639.
26 E. Proietti, F. Jaouen, M. Lefèvre, N. Larouche, J. Tian, J. Herranz and J.-P. Dodelet, *Nat Commun*, 2011, **2**, 416.
27 U. I. Kramm, J. Herranz, N. Larouche, T. M. Arruda, M. Lefevre, F. Jaouen, P. Bogdanoff, S. Fiechter, I. Abs-Wurmbach, S. Mukerjee and J.-P. Dodelet, *Phys. Chem. Chem. Phys.*, 2012, **14**, 11673-11688.
28 N. Larouche, R. Chenitz, M. Lefèvre, E. Proietti and J.-P. Dodelet, *Electrochim. Acta*, 2014, **115**, 170-182.
29 L. Yang, N. Larouche, R. Chenitz, G. Zhang, M. Lefèvre and J.-P. Dodelet, *Electrochim. Acta*, 2015, **159**, 184-197.
30 Y. Zhao, K. Watanabe and K. Hashimoto, *J. Am. Chem. Soc.*, 2012, **134**, 19528-19531.
31 J. M. Ziegelbauer, T. S. Olson, S. Pylypenko, F. Alamgir, C. Jaye, P. Atanassov and S. Mukerjee, *J. Phys. Chem. C*, 2008, **112**, 8839-8849.
32 J. Herranz, F. Jaouen, M. Lefèvre, U. I. Kramm, E. Proietti, J.-P. Dodelet, P. Bogdanoff, S. Fiechter, I. Abs-Wurmbach, P. Bertrand, T. M. Arruda and S. Mukerjee, *J. Phys. Chem. C*, 2011, **115**, 16087-16097.
33 N. Ramaswamy and S. Mukerjee, *Adv. Phys. Chem.*, 2012, **2012**, 491604-491621.
34 X. Li, G. Liu and B. N. Popov, *J. Power Sources*, 2010, **195**, 6373-6378.
35 X. Li, B. N. Popov, T. Kawahara and H. Yanagi, *J. Power Sources*, 2011, **196**, 1717-1722.
36 U. Tylus, Q. Jia, K. Strickland, N. Ramaswamy, A. Serov, P. Atanassov and S. Mukerjee, *J. Phys. Chem. C*, 2014, **118**, 8999-9008.
37 V. Nallathambi, J.-W. Lee, S. P. Kumaraguru, G. Wu and B. N. Popov, *J. Power Sources*, 2008, **183**, 34-42.
38 G. Liu, X. Li, P. Ganesan and B. N. Popov, *Appl. Catal. B: Environ.*, 2009, **93**, 156-165.
39 J. Chen, X. Cui and W. Zheng, *Catal. Commun.*, 2015, **60**, 37-41.
40 J. Y. Cheon, T. Kim, Y. Choi, H. Y. Jeong, M. G. Kim, Y. J. Sa, J. Kim, Z. Lee, T. H. Yang, K. Kwon, O. Terasaki, G. G. Park, R. R. Adzic and S. H. Joo, *Sci Rep*, 2013, **3**, 2715.
41 F. Jaouen, V. Goellner, M. Lefèvre, J. Herranz, E. Proietti and J. P. Dodelet, *Electrochim. Acta*, 2013, **87**, 619-628.
42 A. H. Lu and F. Schüth, *Adv. Mater.*, 2006, **18**, 1793-1805.
43 S. H. Joo, H. I. Lee, D. J. You, K. Kwon, J. H. Kim, Y. S. Choi, M. Kang, J. M. Kim, C. Pak, H. Chang and D. Seung, *Carbon*, 2008, **46**, 2034-2045.
44 H. Chang, S. H. Joo and C. Pak, *J. Mater. Chem.*, 2007, **17**, 3078-3088.
45 J. Zhang, X. Wang, C. Wu, H. Wang, B. Yi and H. Zhang, *React. Kinet. Catal. Lett.*, 2004, **83**, 229-236.
46 J. Zeng, J. Y. Lee and W. Zhou, *Appl. Catal. A: Gen.*, 2006, **308**, 99-104.
47 J. Chen, C. Jiang, X. Yang, L. Feng, E. B. Gallogly and R. Wang, *Electrochem. Commun.*, 2011, **13**, 314-316.
48 B. Ravela and M. Newville, *J. Synchrotron Rad.*, 2005, **12**, 537-541.
49 M. Newville, *J. Synchrotron Rad.*, 2001, **8**, 322-324.
50 J. J. Rehr and R. C. Albers, *Phys. Rev. B*, 1990, **41**, 8139-8149.
51 J. J. Rehr and R. C. Albers, *Reviews of Modern Physics*, 2000, **72**, 621-654.
52 Y. Garsany, I. L. Singer and K. E. Swider-Lyons, *Journal of Electroanalytical Chemistry*, 2011, **662**, 396-406.
53 G. Kresse and J. Furthmüller, *Phys. Rev. B*, 1996, **54**, 11169-11186.
54 G. Kresse and J. Hafner, *Phys. Rev. B*, 1993, **47**, 558-561.
55 P. E. Blöchl, *Phys. Rev. B*, 1994, **50**, 17953-17979.
56 J. P. Perdew, K. Burke and M. Ernzerhof, *Phys. Rev. Lett.*, 1996, **77**, 3865-3868.

57 H. J. Monkhorst and J. D. Pack, *Phys. Rev. B*, 1976, **13**, 5188-5192.
58 K. A. Kuttiyiel, K. Sasaki, Y. Choi, D. Su, P. Liu and R. R. Adzic, *Energy Environ. Sci.*, 2012, **5**, 5297-5304.
59 Y. Jiang, J. B. Adams and M. van Schilfgaarde, *J. Chem. Phys.*, 2005, **123**, 064701.
60 K. A. Kuttiyiel, Y. Choi, S.-M. Hwang, G.-G. Park, T.-H. Yang, D. Su, K. Sasaki, P. Liu and R. R. Adzic, *Nano Energy*, 2015, **13**, 442-449.
61 J. X. Wang, H. Inada, L. Wu, Y. Zhu, Y. Choi, P. Liu, W.-P. Zhou and R. R. Adzic, *J. Am. Chem. Soc.*, 2009, **131**, 17298-17302.

Graphical Abstract